

A stable extended FDTD thin-wire model for lossy wire structures with irregular cross sections

Binghao Li, Yaping Du, Yang Zhang, Jinxing Cao and Mingli Chen

*Dept. of Building Services Engineering, The Hong Kong Polytechnic University
Hung Hom, Kowloon, Hong Kong*

Abstract — A stable extended FDTD thin-wire model for lossy wire structures with irregular cross sections is presented for lightning transient analysis. In this model, the electromagnetic field in the vicinity of a conductor with an irregular cross section is taken into account by adopting a single constant correction factor, and the conductor loss is represented with an internal impedance. These two parameters are calculated with a charge simulation method and an equivalent circuit method, respectively. The proposed model is validated in terms of the characteristic impedance, conductor loss and time-domain waveform with analytical and numerical methods. Good agreements are observed. Considering the rigid conductor-size/cell-size requirement and 8 tedious convolutional processes in the existing non-circular thin-wire model, the implementation complexity of this proposed model is significantly simplified, and the computational stability is remarkably enhanced. Without reducing the time step, the simulation can maintain its stability when the conductor size varies from 0.01 to 1 of the FDTD cell size. It is also revealed that using a single intrinsic model for conductors with different cross sections could lead to significant calculation errors. Finally, this proposed model is applied for the lightning transient analysis in an electrified railway system.

Keywords—Finite-difference time-domain (FDTD), thin wire model, irregular cross section, frequency-dependent loss

I. INTRODUCTION

The finite-difference time-domain (FDTD) method [1] is one of the most widely used numerical methods for analyzing transient behaviors in the time domain. The FDTD method discretizes the whole working volume into a series of cubic cells. With a uniform electromagnetic (EM) field distribution in each cell, the numerical simulation can be performed using the classical Maxwell's equations directly. This method has the advantages of broadband simulation, easy implementation, high stability and parallel computation. Note that the cell size in the classical FDTD method must be smaller than the size of simulated structures. In the case of long conductors whose cross-sectional size is much less than their length, an extremely dense FDTD mesh is required. This could decrease the computation efficiency dramatically.

The thin-wire model is one way to solve this problem. This model constructs an equivalent thin-wire structure with circular cross section in a coarse FDTD mesh. The desired cross-sectional radius can be obtained by modifying either in-cell inductances [2] or correction factors [3-5]. Lossless thin-wire conductors with coaxial structures are modeled in [6]. The internal structure is described with the transmission line theory. The frequency-dependent loss of coaxial cables is taken into consideration in [7, 8]. Note, the aforementioned thin-wire models can only simulate thin conductors with a circular cross section.

In [9], a novel thin-wire model is proposed for long conductors with non-circular cross sections. However, this model is inconvenient to implement. In order to simulate the EM field distribution near a conductor accurately, 4 electric and 4 magnetic field correction factors are determined by using the line-surface averaged concept [5]. The frequency-dependent loss of the non-circular conductor is represented by 4 electric field components in the longitudinal direction. These correction factors and electric field components are not axially symmetric, and have to be calculated separately. Besides, the magnetic correction factors and longitudinal electric field components are frequency dependent. 8 convolutional processes are required in each iteration of the updating process. Furthermore, the requirements for the model stability are strict. The size and orientation of the conductor cross section are restricted in a narrow range with respect to the FDTD cell size, and the time step may be reduced significantly to maintain a stable calculation.

In this paper, a stable extended FDTD thin-wire model is presented for lossy wire structures with irregular cross sections. The EM field near long conductors is described using a single constant correction factor, which can be obtained with the charge simulation method (CSM) numerically. The conductor loss is expressed as a single internal impedance which is calculated with an equivalent circuit method (ECM). The frequency-dependent parameters are considered in the time-domain simulation. The constant correction factors and internal impedances need to be only calculated once prior to the FDTD updating iteration. The rest of this paper is organized as follows. The proposed FDTD thin-wire model is introduced in Section II. Section III describes the derivation of the correction factor and conductor loss component. The proposed model is validated in terms of the characteristic impedance, conductor loss and time-domain waveform in Section IV. An analysis of induced current in a closed-loop circuit made of the non-circular conductor is presented in Section 5. Finally, the proposed thin-wire model is applied to analyze lightning transients in an electrified railway system.

II. THE EXTENDED FDTD THIN-WIRE MODEL

In the FDTD working volume, the EM field associated with a long conductor can be divided into three parts: 1) the EM field inside the conductor, 2) the EM field between the conductor surface and the closed FDTD surface of adjacent cells, and 3) the EM field outside the closed FDTD cell surface.

The effect of the EM field inside the conductor can be described with a lumped internal impedance Z_{int} . The

voltage drop, caused by the internal impedance along the long conductor, is presented in the FDTD region as a series of longitudinal E field components, E_l , as shown in Fig. 1. Δl denotes the FDTD cell size. For a lossless conductor, Z_{int} is equal to zero, and E_l is simply enforced to zero. For a conductor with finite conductivity, Z_{int} is frequency-dependent, and is generally determined by an approach presented in Section III(B). Z_{int} can be approximated by a set of rational functions in s domain with the vector fitting technique [10]. With the time-domain impulse response Z_{int}^* of these functions, E_l can be calculated using a convolutional process as

$$E_l(t) = I_{tot}(t) * Z_{int}^*(t) \quad (1)$$

where I_{tot} is the total current of the conductor.

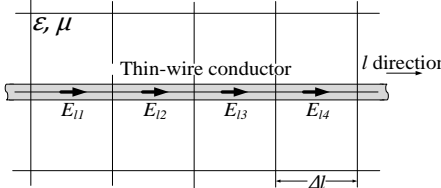


Fig. 1 Conductor internal impedance representation in the FDTD region

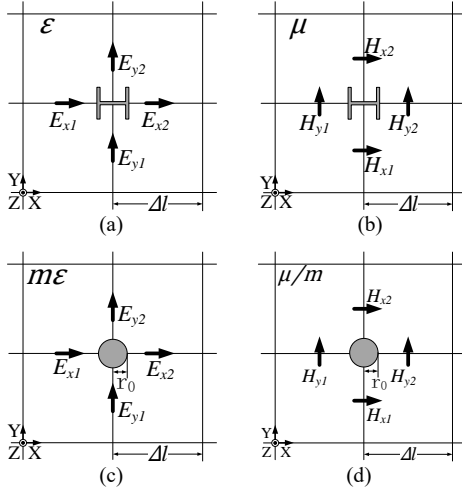


Fig. 2 EM field components between the thin conductor and the closed FDTD surface in the FDTD region

The 3rd part of the EM field is located at least Δl away from the conductor, where its distribution is similar to that generated from a circular conductor. This region is discretized with the FDTD mesh, and the EM field is evaluated with the normal FDTD updating iterations automatically. The 2nd part of the EM field lies between the conductor surface and the closed surface of the FDTD cells. Although the EM field distribution here is irregular because of its irregular cross section, the E field on the closed-cell surface is similar to that generated from a circular conductor. An equivalent circular conductor then is proposed to substitute the non-circular conductor. This region is discretized with 4 coarse FDTD cells in the transverse direction. Fig. 2 (a) and (b) show a conductor with an irregular cross section. Fig. 2 (c) and (d) show its equivalent conductor with intrinsic radius r_0 and modified material parameters $m\epsilon$ and μ/m . Intrinsic radius r_0 is determined by cell size, and is derived numerically [4, 11] or analytically [5]. m is the correction factor to be

determined according to the equivalence of these two conductors.

Consider a virtual cylindrical surface in the FDTD cell with a radius Δl , as shown in Fig. 3. The mutual capacitance between the conductor and cylindrical surface in these two cases is the same, as well as the inductance. Let C_{Mu} and L_{Mu} be the unit-length capacitance and inductance associated with the irregular conductor, which are determined by the procedure given in Section III (A). The following equations then are obtained,

$$C_{Mu} = mC_{Mu.0} \quad (2a)$$

$$L_{Mu} = \frac{L_{Mu.0}}{m} \quad (2b)$$

where both $C_{Mu.0}$ and $L_{Mu.0}$ are the unit-length mutual capacitance and inductance of an intrinsic FDTD thin-wire model in free space. The intrinsic capacitance is expressed as

$$C_{Mu.0} = \frac{2\pi\epsilon_0}{\ln(\Delta l/r_0)} \quad (3)$$

With (3), correction factor m can be directly obtained from (2a). Note that this correction factor is constant and identical in the 4 radial directions. Because of the symmetric structure of the equivalent conductor model, the stability performance of a non-circular thin-wire model is improved, and as good as the circular thin-wire model [12].

III. PARAMETER DETERMINATION

A. Capacitance and inductance per unit length

For a long conductor with circular cross section, the capacitance between the conductor surface and the cylindrical surface can be derived analytically as,

$$C_{Mu} = \frac{2\pi\epsilon}{\ln(\Delta l/r_d)} \quad (5)$$

where r_d is the radius of the conductor.

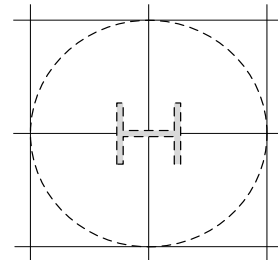


Fig. 3 Discretization of the conductor cross section for the capacitance calculation between the conductor surface and the cylindrical surface

For the long conductor with a non-circular cross section, the CSM [13] is applied to determine the capacitance. Fig. 3 shows the cross section of an arbitrary conductor and a cylindrical surface. Under quasi-static conditions, electric charge is situated on the surface of a conductor and is independent of frequency and conductivity. Assuming the charge carried by the conductor surface per unit length is Q , and the cylindrical surface carries $-Q$. Two surfaces are divided into N elements along transverse boundaries. The charge density in each element is regarded as constant.

Assume charge q_j situates on element s_j with transverse length L_j . With an arbitrary reference point located faraway (its radial distance is much greater than wire cross-sectional dimensions), electric potential ϕ_i (transverse voltage) on the center of element s_i is calculated, as follow:

$$\phi_i = \sum_{j=1}^N \frac{q_j}{2\pi\epsilon L_j} \int_{s_j} \ln \frac{1}{\rho_{i,j}} dl_j = \sum_{j=1}^N P_{i,j} q_j \quad (6)$$

where $\rho_{i,j}$ is the distance between the point in the source element and the middle point of the observation element. $P_{i,j}$ is a potential coefficient between the source and observation cells. A matrix equation for potential vector $\boldsymbol{\phi}$ and charge vector \mathbf{q} on the surfaces is established below,

$$\begin{bmatrix} \mathbf{P}_{CC} & \mathbf{P}_{CB} \\ \mathbf{P}_{BC} & \mathbf{P}_{BB} \end{bmatrix} \begin{bmatrix} \mathbf{q} \\ -\mathbf{q} \end{bmatrix} = \begin{bmatrix} \boldsymbol{\phi}_C \\ \boldsymbol{\phi}_B \end{bmatrix} \quad (7)$$

where \mathbf{P}_{CC} and \mathbf{P}_{BB} are the self-potential coefficient sub-matrices of the conductor and the cylindrical surface. \mathbf{P}_{CB} and \mathbf{P}_{BC} are the mutual-potential coefficient sub-matrices between two surfaces. Note that the potential is the same everywhere on each surface. Let these potentials be ϕ_C and ϕ_B . By performing elementary operations on (7), the surface charge is expressed by

$$\begin{bmatrix} Q \\ -Q \end{bmatrix} = \begin{bmatrix} \beta_{CC} & \beta_{CB} \\ \beta_{BC} & \beta_{BB} \end{bmatrix} \begin{bmatrix} \phi_C \\ \phi_B \end{bmatrix} \quad (8)$$

where β_{CC} and β_{BB} are the self-capacitances of the conductor and the cylindrical surfaces. β_{CB} and β_{BC} are the mutual capacitances between the two surfaces. Inverting the capacitance matrix on the right-hand side of (8) and moving it to the left-hand side, the potential coefficient matrix of two surfaces is derived as

$$\begin{bmatrix} \phi_C \\ \phi_B \end{bmatrix} = \begin{bmatrix} P'_{CC} & P'_{CB} \\ P'_{BC} & P'_{BB} \end{bmatrix} \begin{bmatrix} Q \\ -Q \end{bmatrix} \quad (9)$$

Then the capacitance between the conductor and the cylindrical surface is obtained as

$$C_{Mu} = \frac{\phi_C - \phi_B}{Q} = \frac{1}{P'_{CC} + P'_{BB} - P'_{CB} - P'_{BC}} \quad (10)$$

The correction factor can be calculated with (2a).

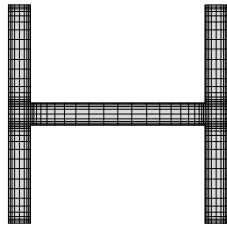


Fig. 4 Cross-sectional discretization for the total impedance calculation

B. Conductor loss

The internal impedance of a circular conductor can be expressed with the Bessel functions [14, 15] as

$$Z_{int} = \frac{j\omega\mu}{2\pi R_d} \cdot \frac{I_0(R_d)}{I_1(R_d)} \quad (11)$$

where $R_d = \gamma r_d$ and $\gamma^2 = j\omega\mu(\sigma + j\omega\epsilon)$. I_n is the modified Bessel function of the first kind at order n .

An analytical formula of internal impedance could not be possibly derived in the case of conductors with non-circular cross sections. In this case, a numerical procedure based on the ECM is applied to determine total impedance Z_{tot} . The internal impedance can be obtained by subtracting the external reactance $j\omega L_{ext}$ from the total impedance of the conductor, as follows:

$$Z_{int} = Z_{tot} - j\omega L_{ext} \quad (12)$$

Consider a nonmagnetic conductor and divide it into M small rectangular elements on its cross section, as shown in Fig. 4. The current density in each element is constant. Under the quasi-static conditions, each element is represented with circuit components: resistance and inductance. With the relationship of electric potential ϕ and magnetic potential A on the conductor, $-\nabla\phi = \mathbf{J}/\sigma + j\omega\mathbf{A}$, a system of equations in the frequency domain can be established,

$$\Delta\boldsymbol{\phi} = \mathbf{Z}_{tot}\mathbf{I} = \mathbf{R}\mathbf{I} + j\omega\mathbf{L}_{tot}\mathbf{I} \quad (13)$$

where $\Delta\boldsymbol{\phi}$ is the potential difference (longitudinal voltage) vector for unit-length elements, and \mathbf{I} is the current vector of these elements. In (13) elements $R_{i,i}$ and $L_{i,j}$ of resistance and inductance matrices \mathbf{R} and \mathbf{L}_{tot} are given by

$$R_{i,i} = \frac{1}{\sigma\Delta s_i} \quad (14a)$$

$$L_{i,j} = \frac{j\omega\mu_0}{2\pi\Delta s_j} \int_{s_j} \ln \frac{1}{\rho_{i,j}} ds_j \quad (14b)$$

where Δs_j is the area of the j th element s_j . As the potential difference of these elements is identical, the total admittance can be obtained by inverting the total impedance matrix and summing up all the elements, as follows

$$I_{tot} = Y_{sum}V \quad (15)$$

where Y_{sum} is the summation of all elements in matrix \mathbf{Z}_{tot}^{-1} . Then the total impedance yields

$$Z_{tot} = Y_{sum}^{-1} \quad (16)$$

The formulation for magnetic conductors is given in the Appendix.

The external inductance of the thin-wire conductor with an arbitrary reference line located far away is frequency-independent. With the self-capacitance coefficient of the conductor, β_{CC} , in (8), the external inductance is expressed as [16]

$$L_{Ext} = \frac{1}{v^2\beta_{CC}} \quad (17)$$

where v is the wave propagation speed. Substituting (16) and (17) into (12) yields the frequency-dependent internal impedance of a long conductor with a non-circular cross section.

IV. VALIDATIONS

For validation, the characteristic impedance, loss of long conductors and time-domain waveforms, evaluated by the

proposed thin-wire model, are compared with the CSM, the transmission line theory (TLT) and the traditional FDTD method. Six different cross-sectional shapes of the conductor are selected for comparison, i.e., rectangular shape, L shape, T shape, H shape, U shape and cruciform, as shown in Fig. 5. The conductivity, relative permittivity and permeability of the lossy conductor material are assigned as $5e6$ S/m, 1 and 200 [17].

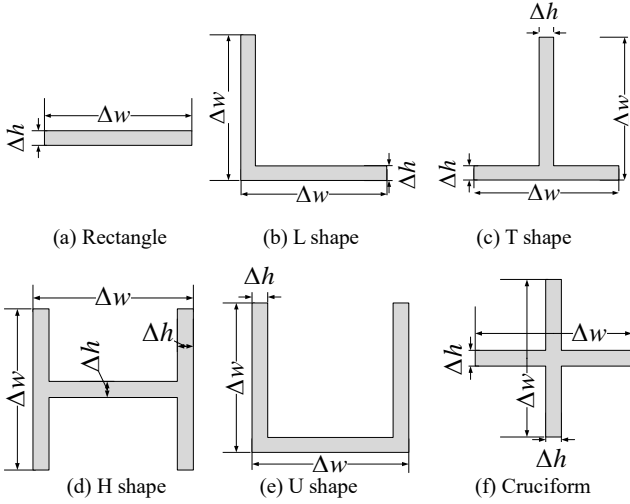


Fig. 5 Six cross sectional shapes of a long conductor

The system configuration for the first two validations is shown in Fig. 6. A long and thin conductor with a length of 1 km, is arranged 2 m above a perfect ground. The left side of the conductor is connected to the ground via a lossless wire and an ideal current source. The right side of the conductor is left open. In the FDTD region, the cell size is defined as 0.5 m universally. The time step is set as 0.96225 ns to meet the Courant-Friedrich-Levy (CFL) limit. The perfect electric conductor (PEC) condition is applied to the bottom boundary of the FDTD region to simulate the perfect ground. The other boundaries are covered with perfectly matched layers (PML) to absorb unwanted reflections.

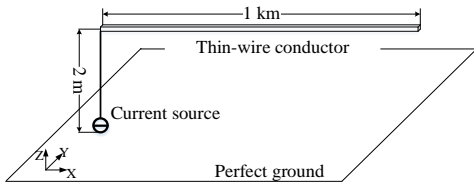


Fig.6 Configuration of the analytical validation arrangement

A. Characteristic impedance

The steady-state characteristic impedances of lossless conductors with respect to the PEC ground is compared with the results obtained from the CSM. CSM discretizes the cross-sectional surface of the conductor and its image surface to evaluate inductance, L_{CSM} , and capacitance, C_{CSM} , per unit length numerically. Then the steady-state characteristic impedance, Z_{CSM} , can be determined as

$$Z_{CSM} = \sqrt{L_{CSM}/C_{CSM}} \quad (18)$$

In the FDTD region, the source generates a unit step current with a $0.02 \mu\text{s}$ rising time. Both the steady-state conductor current, I_{FDTD} , and the conductor-to-ground voltage, V_{FDTD} , are measured 10 m away from the current

source, before the reflected wave from its far end arrives. The characteristic impedance in the FDTD region then is determined as

$$Z_{FDTD} = V_{FDTD}/I_{FDTD} \quad (19)$$

The width-to-thickness ratio of the conductor, i.e. $\Delta w/\Delta h$, is fixed as 10 in the simulation. While the ratio of conductor width to the FDTD cell size, $r = \Delta w/\Delta l$, is changed from 0.01 to 1, i.e. the cross-sectional width of the conductor varies from 5 mm to 500 mm. This test is designed to analyze the accuracy of the proposed thin-wire model for the conductors with different cross-sectional sizes.

Table 1 Steady-state characteristic impedance values for lossless thin-wire conductors with non-circular cross sections calculated by the proposed model and the CSM ($\Delta w/\Delta h = 10, \Delta w/\Delta l = r, \Delta l = 0.5\text{m}$)

Type	Method	Characteristic impedance / ohm				Average Error
		$r=0.01$	$r=0.1$	$r=0.5$	$r=1$	
Rect.	CSM	473.5	335.4	238.9	197.5	0.55%
	Prop.	467.3	332.8	238.6	197.5	
L shape	CSM	446.4	308.0	211.4	169.7	0.86%
	Prop.	440.6	306.0	211.1	167.4	
T shape	CSM	449.8	311.4	214.8	173.1	0.65%
	Prop.	443.9	309.4	214.8	172.0	
H shape	CSM	435.6	297.6	201.0	159.1	0.77%
	Prop.	430.5	295.9	201.7	160.7	
U shape	CSM	434.3	296.0	199.4	157.7	0.77%
	Prop.	428.9	294.4	200.1	159.2	
Cruciform	CSM	455.4	317.3	220.8	179.1	0.67%
	Prop.	449.7	315.1	220.9	180.3	

The characteristic impedance of lossless conductors calculated by the proposed thin-wire model and the CSM are listed in Table 1. It is found that the average and maximum errors are 0.61% and 1.35%. Good agreements are observed. This indicates that the characteristic impedance of the proposed thin-wire model for lossless conductors with irregular cross sections is accurate.

Table 2 Reduction factor (RF) adopted in the existing and proposed thin-wire models for lossy and lossless thin-wire conductors ($\Delta w/\Delta h = 10, \Delta w/\Delta l = r, \Delta l = 0.5\text{m}$)

Type	Conductor case	Reduction factors (RF)			
		$r=0.01$	$r=0.1$	$r=0.5$	$r=1$
Existing thin-wire model					
Rect.	Lossless	1	1	1	\
	Lossy	0.7	0.8	<0.1	\
L shape	Lossless	1	1	1	\
	Lossy	0.1	0.9	<0.1	\
T shape	Lossless	1	1	1	\
	Lossy	<0.1	0.1	<0.1	\
Proposed thin-wire model					
Rect.	Lossless	1	1	1	1
	Lossy	1	1	1	1
L shape	Lossless	1	1	1	1
	Lossy	1	1	1	1
T shape	Lossless	1	1	1	1
	Lossy	1	1	1	1

The stability performance of the proposed thin-wire model also is investigated by comparing that of the existing non-circular thin-wire model [9]. A reduction factor RF is introduced to determine the upper limit of the FDTD time step Δt for stable computation, as follows:

$$\Delta t < RF \times \Delta t_{CFL} \quad (20)$$

where Δt_{CFL} is the CFL time step limit. The adopted RF in the existing and proposed models for lossy and lossless thin-wire conductors are listed in Table 2.

The stability performance of the existing thin-wire model for lossless cases is generally acceptable. However, in some lossy conductor cases, the RF is lower than 0.1. This is unrealistic in the practical simulation due to its low calculation efficiency. Furthermore, the existing non-circular model cannot simulate the case of $r \geq 1$, because the cross-sectional size exceeds the effective region [9]. Compared to the existing non-circular thin-wire model, the proposed thin-wire model has much better stability performance. The simulation can maintain stability with the RF of 1 in both lossy and lossless conductor cases. In other words, the simulation can maintain stability without reducing the time step even if the size of the cross section varies from 5 mm to 500 mm for the fixed cell size of 500 mm.

B. Conductor loss

The conductive loss of the conductor is simulated with the proposed model, and a comparison is made by using the TLT. The configuration shown in Fig. 6 is adopted. The conductor has a width of $\Delta w = 250$ mm and a height of $\Delta h = 25$ mm. The source generates a sinusoidal current at 5 MHz or 10 MHz in the test, for checking the broadband characteristics of the proposed thin-wire model. The current amplitude at $x = 100$ m is assumed to be 1 kA. The current amplitudes at four locations are calculated for comparison, i.e., $x = 200$ m, 300 m, 400 m and 500 m. The reflected wave from the far end is not included in the calculation.

The current along the long conductor at an angular frequency ω can be calculated theoretically by

$$I(x, t) = I_0 e^{\alpha x} \sin(\omega t - \beta x) \quad (21)$$

where parameters α and β are expressed with frequency-dependent L and R , and frequency-independent C as

$$\alpha = \sqrt{[(\omega^2 LC)^2 + (\omega RC)^2]^{1/2} - \omega^2 LC} / \sqrt{2}$$

$$\beta = \sqrt{[(\omega^2 LC)^2 + (\omega RC)^2]^{1/2} + \omega^2 LC} / \sqrt{2}$$

The resistance, inductance and capacitance of the long conductor with respect to the perfect ground can be evaluated with the CSM and the ECM, and are listed in Table 3.

Table 3 L, R and C of the conductors with different non-circular cross sectional shapes, 2 m above a PEC ground calculated by the CSM and the ECM (frequency = 5 MHz or 10 MHz)

Type	Freq./MHz	L/ μ H	R/ Ω	C/pF
Rect.	5	1.2654	0.6559	9.9451
	10	1.2246	0.9547	
L shape	5	1.1249	0.4315	10.8311
	10	1.0978	0.6307	
T shape	5	1.1438	0.4537	10.7114
	10	1.1149	0.6678	
H shape	5	1.0768	0.3635	11.2088
	10	1.0535	0.5353	
U shape	5	1.0650	0.3491	11.2689
	10	1.0433	0.5080	
Cruciform	5	1.1745	0.4820	10.5127
	10	1.1428	0.7178	

The current amplitudes along the conductor are calculated with these two methods. The results at four locations are listed in Tables 4 and 5. It is observed that the

current amplitude decreases to around 70% of the original amplitude at a distance of 500 m in all cases. The average and maximum relative errors of the amplitudes are respectively 0.96% and 2.66%. This indicates that the proposed thin-wire model can simulate the frequency-dependent conductor loss with satisfactory accuracy.

Table 4 Current amplitude calculated by the proposed thin wire model and TLT (Frequency=5 MHz)

Type	Method	Current/A				Average error
		200m	300m	400m	500m	
Rect.	TLT	912.2	832	759	692.3	1.66%
	Prop.	906.1	820.9	743.8	673.9	
L shape	TLT	935.2	874.7	818.0	765.1	0.98%
	Prop.	931.5	867.8	808.4	753.1	
T shape	TLT	932.9	870.4	812.0	757.5	1.07%
	Prop.	928.9	862.8	801.5	744.6	
H shape	TLT	943.0	889.3	838.7	790.9	0.79%
	Prop.	940.0	883.7	830.7	780.9	
U shape	TLT	944.8	892.6	843.4	796.8	0.72%
	Prop.	942.0	887.5	836.1	787.7	
Cruciform	TLT	930.4	865.7	805.5	749.5	1.20%
	Prop.	925.9	857.4	793.9	735.2	

Table 5 Current amplitude calculated by the proposed thin wire model and TLT (Frequency=10 MHz)

Type	Method	Current/A				Average error
		200m	300m	400m	500m	
Rect.	TLT	872.8	761.8	664.9	580.3	1.49%
	Prop.	867.6	752.8	653.1	566.4	
L shape	TLT	905.7	820.3	742.9	672.9	0.71%
	Prop.	903.2	815.6	736.7	665.2	
T shape	TLT	901.7	813.0	733.1	661.0	0.83%
	Prop.	898.7	807.8	725.8	652.1	
H shape	TLT	916.4	839.8	769.6	705.2	0.56%
	Prop.	914.2	836.1	764.4	698.9	
U shape	TLT	919.9	846.2	778.5	716.1	0.52%
	Prop.	917.9	842.9	773.6	710.2	
Cruciform	TLT	896.9	804.4	721.4	647.0	0.96%
	Prop.	893.5	798.1	713.2	637.1	

C. Time-domain waveform

The traditional FDTD method, which discretizes the wire structures with a dense FDTD meshing scheme, are adopted to validate the proposed thin-wire model in the time domain. Fig. 7 shows the testing configuration. Two conductors with L-shape cross sections are fed by a voltage source in free space. The geometrical structure of the cross section is shown in Fig. 5 (b), where $\Delta w = 3$ mm and $\Delta h = 0.3$ mm. The length of each conductor is 2 m. The voltage source generates a 1 V Gaussian pulse waveform ($\sigma = 1.5 \times 10^{-9}$, $\mu = 5 \times 10^{-9}$).

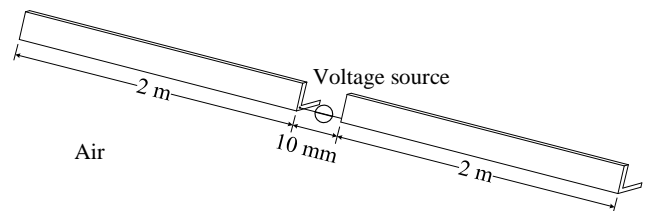


Fig. 7 Configuration of the time-domain validation

The current at the feeding point is simulated with three methods, including the traditional FDTD method, the existing thin-wire model and the proposed thin-wire model. In the traditional FDTD method, a non-uniform meshing scheme is adopted. The minimum cell size, $0.05\text{mm} \times 0.05\text{mm} \times 5\text{mm}$, is defined near the conductors to consider

the frequency-dependent loss. In both the existing and proposed models, a uniform meshing scheme is adopted. Two cell sizes, $\Delta l = 5\text{mm}$ and $\Delta l = 10\text{mm}$, are selected in the proposed model for validating the model accuracy. Only the cell size of 10 mm is selected in the existing model due to its limitation shown in Table 2. To accelerate numerical computation, a graphics processing unit (NVIDIA® Tesla™ K40C GPU Computing Accelerator) is employed.

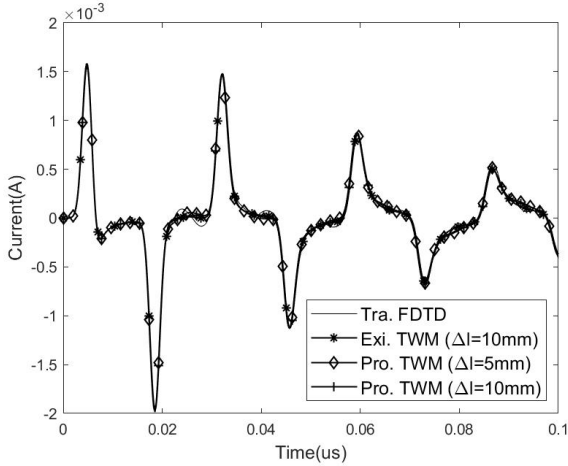


Fig. 8 Current flow through the voltage source

Table 6 Computational information of the three methods

Method	Time step	Simulation time	Required memory
Traditional FDTD	2.3586e-14 s	97 h 48 m	10.30 GB
Proposed TWM ($\Delta l = 5\text{mm}$)	9.6225e-12 s	11 m	2.65 GB
Proposed TWM ($\Delta l = 10\text{mm}$)	1.9245e-11 s	4 m	1.98 GB
Existing TWM ($\Delta l = 5\text{mm}$)	\	\	\
Existing TWM ($\Delta l = 10\text{mm}$)	1.7320e-11 s	16 m	1.99 GB

Fig. 8 shows the current at the feeding point calculated with three methods. It is observed that the current waveforms match well. The maximum relative errors of the proposed thin-wire model with 5 mm and 10 mm cell sizes are 2.15% and 2.96%. The time steps, simulation time and memory space consumption are summarized in Table 6. Compared to the traditional FDTD method, the proposed thin-wire model with 5/10 mm cell sizes saves 99.71%/99.93% of simulation time, and 74.27%/80.78% memory space. It is shown that the proposed thin-wire model can simulate current waveforms in the time domain accurately with high computational efficiency.

The accuracy and efficiency of the existing thin-wire model with a 10 mm cell size is also acceptable compared with the traditional FDTD method. The maximum relative error of the existing thin-wire model is 3.08%. However, since the 8 convolutional processes during each updating procedure per unit length, the simulation time of the existing model is 4 times longer than the proposed one. Furthermore, when the cell size is defined as 5 mm, the time step of the existing model should be at least 10 times less than the CFL time step limit, which is unacceptable in this case. Clearly,

the proposed thin-wire model has much better performance than the existing model.

V. INFLUENCE OF GEOMETRIC AND MATERIAL PARAMETERS OF CROSS-SECTIONAL SHAPE

Conductors or metallic components used in practical systems can have different cross-sectional shapes, as illustrated in previous sections. Their geometric and material parameters affect the external impedances and internal impedances of the conductors, subsequently the lightning transient in the system. Modeling different types of conductors in the FDTD region with an intrinsic thin-wire model, without modifying corresponding material parameters, may affect calculation accuracy. In this section, this issue is investigated by examining the induced current in a closed-loop circuit made by a non-circular conductor.

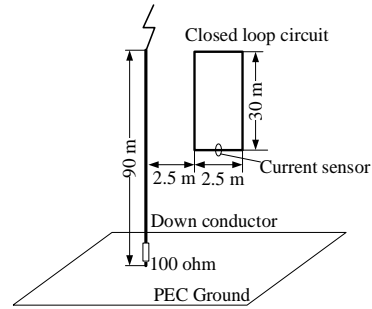


Fig. 9 Configuration for the induced current simulation

Fig. 9 illustrates the configuration for a lightning transient analysis used in [18]. A 90-meter-long lossless down conductor with an intrinsic circular cross section is erected vertically above the ground. It is connected to the ground via a lumped resistance of 100 ohm and is struck by lightning at the upper end. A 2.5 m \times 30 m closed conductor loop is placed 60 m above the ground and 2.5 m away from the down conductor. The loop is made of the conductor with an L-shape cross section and is modeled in the FDTD region with the proposed thin-wire model. The conductivity, relative permittivity and permeability of the lossy wire conductor are $5\text{e-}6\text{ S/m}$, 1 and 200. Different cross-sectional sizes under lossy/lossless conductor scenarios are simulated. The lightning return stroke is represented as a current source together with an upward wire extended to the PML boundary. It generates a 1.2/50 μs impulse current with an amplitude of 1 kA. The size of the FDTD cells is fixed to be 0.5 m universally. The induced current is measured at the lower end of the conductor loop.

Fig. 10 shows the induced currents in the loop made by the L-shape conductor with the widths of 5 mm, 50 mm, 250 mm and 500 mm, respectively. It is observed that the wavefront of all the currents is similar in both the lossless and lossy cases, but the wave tail is significantly different. As seen in Fig. 10, the current decreases rapidly in the wave tail in the lossy cases, but decreases slowly in the lossless cases. The amplitudes of the induced current vary significantly with the cross-sectional size. The results using the circular conductor with an intrinsic radius of $r_0 = 99.5\text{ mm}$ [11] also are presented as a reference for comparison. It is found that the difference in the current amplitude can be up to 134% of that in the reference case if

the conductor width reaches 500 mm. The simulation results show that both the cross-sectional size and conductor material have a significant impact on the induced current waveform and amplitude. Therefore, the cross-sectional size and conductor material of thin-wire conductors should be appropriately considered in FDTD simulations. Representing different types of conductors with a simple intrinsic thin-wire model may lead to a significant simulation error. Note that both the lossless conductor with a width of 250 mm and the intrinsic thin-wire model have a similar induced current.

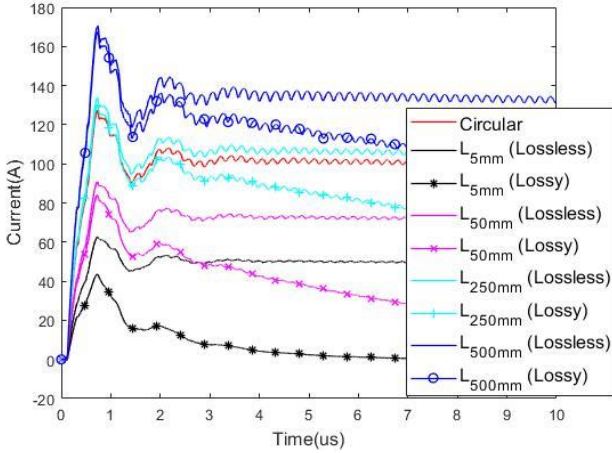


Fig. 10 Simulated current waveforms in the closed-loop circuit

VI. SURGE ANALYSIS IN AN ELECTRIFIED RAIL SYSTEM

The proposed thin-wire model is applied for lightning transient analysis in an electrified railway system. The configuration is illustrated in Fig. 11. The railway rails are separated by 1.5 m and are laid above the ground. The rails do not contact with soil directly. 25 track-side masts with a spacing of 50 m are erected along the line between two passenger stations. These masts have a height of 6 m in the air, and 1-meter deep reinforced concrete foundation underground. The conductivity, relative permittivity and relative permeability of the masts are defined as $5e6$ S/m, 1 and 200. A contact wire (CW) is hinged 5.5 m above the ground surface and is insulated from track-side masts via insulators. The lightning withstand voltage of these insulators is 200 kV. A fault current return wire (FCRW) is installed 2 m away from the track and is bonded to the masts. FCRW is bonded to the rail track as well at masts 1, 13 and 25. The track is grounded at stations A and B with a resistance of lower than 1 ohm.

An axle counter is installed at the trackside between mast 12 and 13 to determine the occupation of this railway block. The signal is transmitted to a control station via a signal cable. The cabinet is bonded via a conductor to the track. Surge protective devices (SPDs) are installed between the signal port and the ground in the cabinet. The signal cable runs 500 m in parallel with and 3 m away from the track and connects the equipment in the control station 50 m away. In the control station, the signal line is grounded via SPDs to a clean earth system. It is found that one SPD in the cabinet is broken in a thunderstorm. The lightning surge current in the SPD then is analyzed in this section.

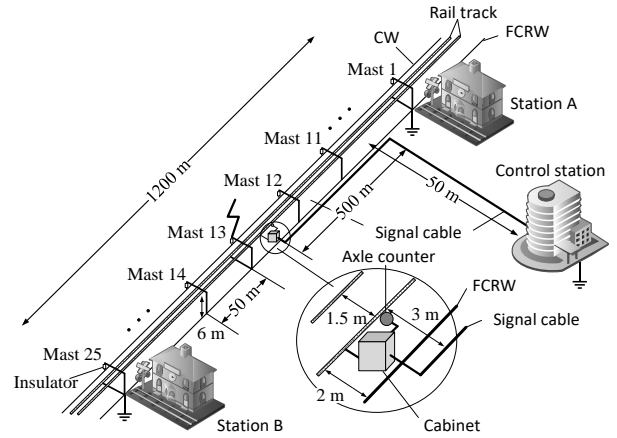


Fig. 11 Configuration of a light rail system

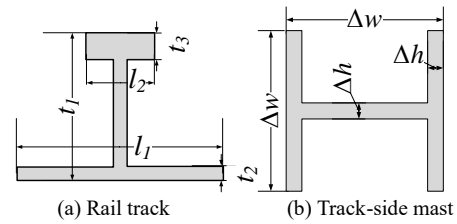
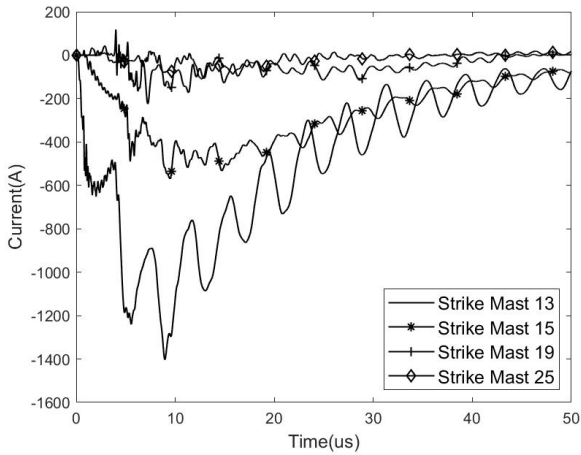


Fig. 12 The cross sections of the rail track and the track-side mast ($l_1=150$ mm, $l_2=75$ mm, $t_1=175$ mm, $t_2=15$ mm, $t_3=35$ mm, $\Delta w=200$ mm, $\Delta h=16$ mm)

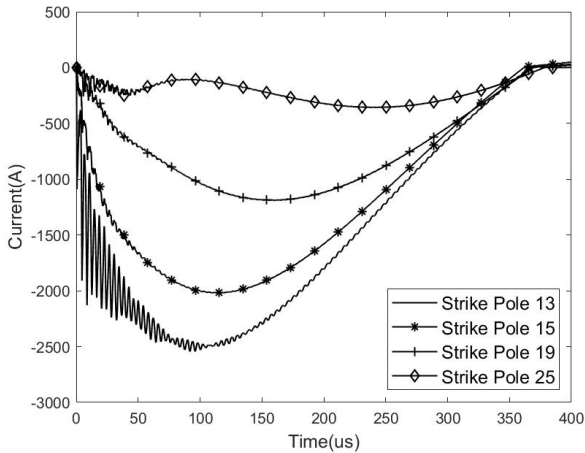
In the simulation, the FDTD working volume consists of $100 \times 340 \times 90$ FDTD cells. The cell size near the axle counter is 0.5 m and increases to 10 m gradually. The rails and the track-side masts are simulated with the proposed thin-wire model. The cross sections of these conductors are shown in Fig. 12. Both the contact wire (CW) and fault current return wire (FCRW) have radii of 6.18 mm and 18.9 mm, respectively. The signal cable is regarded as a solid wire. The conductivity, relative permittivity and relative permeability of the circular thin-wire conductors are $5.96e7$ S/m, 1 and 1. Two far ends of rail tracks, CW and FCRW are attached to the PML absorbing boundaries to simulate an infinite long circuit. The conductivity, relative permittivity and relative permeability of the lossy ground are defined as 0.005 S/m, 10 and 1. The insulators on the masts are represented with a breakdown model. The breakdown voltage is defined as 200 kV [19]. The lightning protection in the axle counter is provided by a metal oxide varistor (MOV) SIOV-S20K150. It can withstand an 8/20 μ s 8kA impulse current, but it will be de-rated if the lightning current has a longer duration [20]. This device in the counter is modeled as an active current source [21]. The engineering return stroke model [22] is adopted to simulate a lightning channel. In the simulations, the lightning strike terminates on a mast directly. The 4/10 μ s impulse current [23] and the first negative lightning current (1/200 μ s) [24] of 46 kA are applied separately. This is the figure that 95% of lightning currents are less than in a time period of 7 years in this area.

The waveforms of the currents in the MOV under two lightning stroke cases are shown in Fig. 13. For a 400 μ s simulation case, it consumes 1.69 GB memory space and run 15 hours and 36 minutes. When the masts 13, 15, 19 and 25 are struck by lightning separately, the surge currents

respectively have the amplitudes of 1404 A, 569 A, 167 A and 225 A under the 4/10 μs return stroke. The time to half peak is less than 20 μs in the worst current case. The MOV can survive in such a case. Under the 1/200 μs return stroke, the surge currents respectively have the amplitudes of 2544 A, 2020 A, 1190 A and 311 A. It is observed that these currents have a very long duration, and the time to half peak is longer than 200 μs . This is much longer than that in the standard 8/20 μs waveform used for testing MOVs. According to the derating curve provided in the datasheet [20], the maximum withstand current of SIOV-S20K150 is reduced to 920 A for a 200 μs pulse current. Therefore, such a metal oxide varistor, which is not damaged under the 4/10 μs lightning return stroke, will be broken in the case of the first negative lightning strike to masts 13 or 15.



(a) under a 46 kA 4/10 μs return stroke

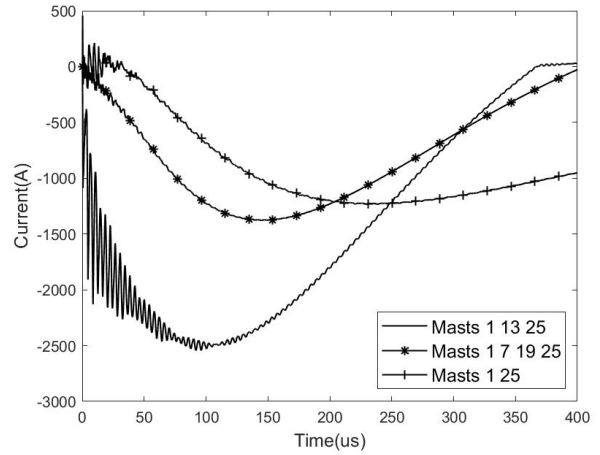


(b) under a 46 kA 1/200 μs return stroke

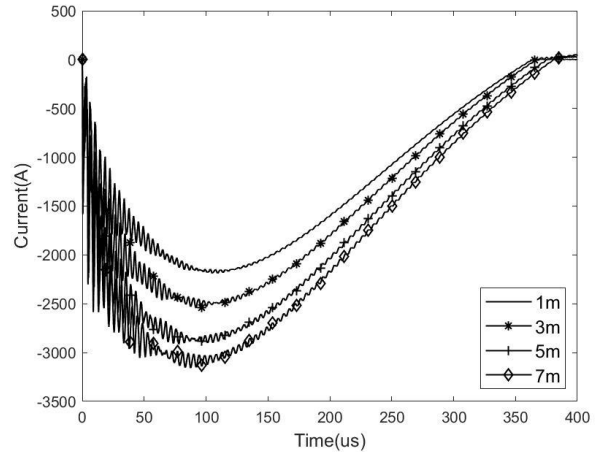
Fig. 13 Surge current in a MOV under two lightning return strokes

The effects of both bonding points and the separation distance between the signal cable and rail tracks then are investigated. The worst case of a 46 kA 1/200 μs return stroke terminated on mast 13 is adopted for the investigation. Firstly, three schemes of bonding points are selected for analysis, i.e., (a) bonding at masts 1, 13 and 25; (b) bonding at masts 1, 7, 19 and 25; (c) bonding at masts 1 and 25. Fig. 14(a) shows the surge currents in the MOV. The current amplitudes are 2544 A, 1377 A and 1235 A. It is found that the surge current is reduced significantly if the bonding point near mast 13 is removed. It is also found that the waveform

is elongated if the number of bonding points is reduced. Fig. 14(b) shows the MOV currents with bonding scheme (a) when the separation distance varies from 1 m to 7 m. It is observed that a short distance can reduce the amplitude of the surge current. This is because the magnetic flux between the signal cable and the rail tracks is decreased. Therefore, the induced surge current in the cable-track loop is reduced.



(a) Different schemes of bonding points



(b) Different distances between the signal cable and rail tracks

Fig. 14 Surge currents in the MOV under a 46 kA 1/200 μs return stroke strikes mast 13

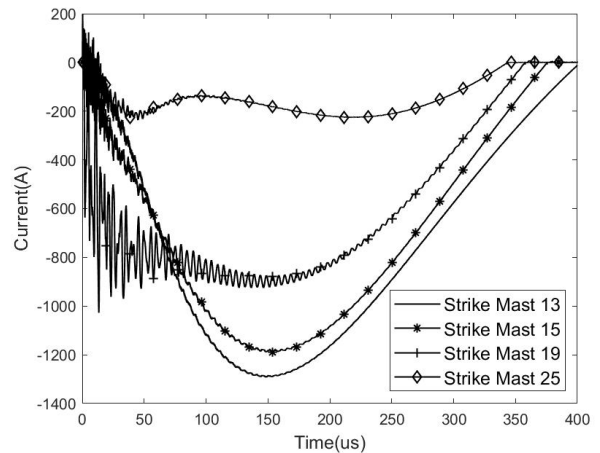


Fig. 15 Surge currents in the MOV with two mitigation measures under a 46 kA 1/200 μs return stroke at different striking points

To mitigate the surge current in the MOV, both the bonding scheme (b) and the separation distance of 1 m are adopted. Fig. 15 shows the surge currents under the 46 kA 1/200 μ s return stroke at different striking points. The surge amplitudes now are reduced to 1293 A, 1190 A, 1027 A and 237 A. It is observed that the surge current is reduced, but it may exceed the withstanding capacity of the MOV model used in the railway. A new MOV model, V151HA32 [25] then is suggested. This type of MOV has similar ratings, but with a higher surge withstand current. According to the derating curve provided in the datasheet [25], the maximum withstand current for a 200 μ s pulse current is 1800 A, which fully satisfies the lightning protection requirements for the electrified railway system.

VII. CONCLUSIONS

A stable extended FDTD thin-wire model for lossy wire structures with irregular cross sections was proposed in this paper. The irregular EM field distribution in the vicinity of such conductors was taken into account by adopting one simple constant correction factor. The constant correction factor was evaluated with the CSM numerically. The conductor loss, as well as the ferromagnetic effect, was modeled using frequency-dependent internal impedance, which was calculated using an ECM. Both the correction factors and internal impedances were only calculated once prior to the FDTD updating iteration. The proposed model was validated analytically and numerically for the conductors with six different cross-sectional shapes. Compared to the existing non-circular thin-wire model, the implementation complexity of the proposed model is noticeably simplified, and the computational stability is remarkably enhanced. The simulation can maintain stability without reducing the time step when the cross-sectional size varies from 0.01 to 1 of the FDTD cell size.

With the proposed model, the influence of the cross-sectional shape under both lossy and lossless scenarios was investigated. It is found that the cross-sectional size and conductor resistance could affect the induced current significantly in a closed-loop circuit. The geometric and material parameters of a conductor should be appropriately considered in FDTD simulations. Using a simple intrinsic thin-wire model to simulate the conductors with different shapes and sizes may lead to significant simulation errors. The proposed thin-wire model was applied for a lightning surge analysis in an electrified railway system. Lightning current in a metal oxide visitor in the track-side equipment was evaluated under a direct lightning strike. It is found that the lightning current in the surge protective device has a relatively long duration. Under a 1/200 μ s lightning return stroke terminated on the track-side mast, track-side devices such as axle counters could be possibly damaged. Removing the bonding point near the axle counter and reducing the distance between the signal cable and rail tracks can reduce the surge current amplitude effectively. A more suitable MOV is also recommended based on the simulation results.

ACKNOWLEDGMENT

The work leading to this paper was supported by grants from the Research Grants Council of the HKSAR (Project No. 152100/17E and 152100/18E) and the Research Committee of HK PolyU.

APPENDIX

In a conductor made of linear magnetic material, the inductive contribution resulting from magnetic polarization has to be included in the voltage equation. According to the constitutive equation for a linear magnetic material, the following matrix equation in terms of element current density (\mathbf{J}_c) and magnetization vector (\mathbf{M}_x and \mathbf{M}_y) is established [26-27] for rectangular elements in a 2D conductor under quasi-static conditions,

$$\begin{bmatrix} \mathbf{Z}_c & j\omega\mathbf{G}_{12} & j\omega\mathbf{G}_{13} & \mathbf{U} \\ \mathbf{G}_{21} & \mathbf{P}_{xx} & \mathbf{G}_{23} & \mathbf{0} \\ \mathbf{G}_{31} & \mathbf{G}_{32} & \mathbf{P}_{yy} & \mathbf{0} \\ \mathbf{S} & \mathbf{0} & \mathbf{0} & 0 \end{bmatrix} \begin{bmatrix} \mathbf{J}_c \\ \mathbf{M}_x \\ \mathbf{M}_y \\ \Delta V \end{bmatrix} = \begin{bmatrix} \mathbf{0} \\ \mathbf{0} \\ \mathbf{0} \\ I_{tot} \end{bmatrix} \quad (A1)$$

where \mathbf{U} is a unit vector and Matrix \mathbf{S} contains the areas of rectangular cells. Entries in the parameter matrix of (A1) are given, as follows:

$$\begin{aligned} \mathbf{Z}_c &= j\omega\mathbf{G}_{11} + \mathbf{E}K_e \\ \mathbf{P}_{xx} &= \mathbf{G}_{22} - \mathbf{E}K_m \\ \mathbf{P}_{yy} &= \mathbf{G}_{33} - \mathbf{E}K_m \\ G_{11.i,j} &= \sum_{j=1}^M \frac{\mu_0}{2\pi\Delta s_j} \int_{s_j} \ln \frac{1}{\rho_{i,j}} ds_j \\ G_{12.i,j} &= -G_{21.i,j} = \sum_{j=1}^M \frac{\mu_0}{2\pi} \int_{s_j} \ln \frac{y_j - y_i}{\rho_{i,j}^2} ds_j \\ G_{13.i,j} &= -G_{31.i,j} = \sum_{j=1}^M \frac{\mu_0}{2\pi} \int_{s_j} \ln \frac{-(x_j - x_i)}{\rho_{i,j}^2} ds_j \\ G_{23.i,j} &= G_{32.i,j} = \sum_{j=1}^M \frac{\mu_0}{2\pi} \int_{s_j} \ln \frac{2(x_j - x_i)(y_j - y_i)}{\rho_{i,j}^4} ds_j \\ G_{22.i,j} &= -G_{33.i,j} \\ &= \sum_{j=1}^M \frac{\mu_0}{2\pi} \int_{s_j} \ln \frac{(x_j - x_i)^2 - (y_j - y_i)^2}{\rho_{i,j}^4} ds_j \end{aligned}$$

where \mathbf{E} is a unit diagonal matrix, $K_e = 1/\sigma$ and $K_m = \mu_0\mu_r/(\mu_r - 1)$. By performing elementary operations similar to those in Section III, the voltage drop on a unit-length conductor, ΔV , can be derived. The frequency-dependent total impedance considering linear ferromagnetism is obtained as

$$Z_{tot} = \frac{I_{tot}}{\Delta V} \quad (A2)$$

REFERENCES

- [1] Yee, K.S., Numerical solution of initial boundary value problems involving Maxwell's equations in isotropic media. IEEE Trans. on AP, 1966. 14(3): p. 302-307.
- [2] Holland, R., et al., Finite-difference analysis of EMP coupling to thin struts and wires. IEEE Trans. on EMC, 1981(2): p. 88-97.
- [3] Umashankar, K.R., et al., Calculation and experimental validation of induced currents on coupled wires in an arbitrary shaped cavity. IEEE Trans. on AP, 1987. 35(11): p. 1248-1257.

- [4] Noda, T. and Yokoyama, S., Thin wire representation in finite difference time domain surge simulation. *IEEE Trans. on PWRD*, 2002. **17**(3): p. 840-847.
- [5] Railton, C.J., et al., The treatment of geometrically small structures in FDTD by the modification of assigned material parameters. *IEEE Trans. on AP*, 2005. **53**(12): p. 4129-4136.
- [6] Tatematsu, A., A technique for representing coaxial cables for FDTD-based surge simulations. *IEEE Trans. on EMC*, 2015. **57**(3): p. 488-495.
- [7] Du, Y., Li, B. and Chen, M., The extended thin-wire model of lossy round wire structures for FDTD simulations. *IEEE Trans. on PWRD*, 2017. **32**(6): p. 2472-2480.
- [8] Tatematsu, A., A Technique for representing lossy thin wires and coaxial cables for FDTD-based surge simulations. *IEEE Trans. on EMC*, 2018. **60**(3): p. 705-715.
- [9] Li, B., Du, Y. and Chen, M., An FDTD thin-wire model for lossy wire structures with noncircular cross section. *IEEE Trans. on PWRD*, 2018. **33**(6): p. 3055-3064.
- [10] Gustavsen, B. and Semlyen, A., Rational approximation of frequency domain responses by vector fitting. *IEEE Trans. on PWRD*, 1999. **14**(3): p. 1052-1061.
- [11] Asada, T., et al., An improved thin wire representation for FDTD transient simulations. *IEEE Trans. on EMC*, 2015. **57**(3): p. 484-487.
- [12] Taniguchi, Y., et al., An improved thin wire representation for FDTD computations. *IEEE Trans. on AP*, 2008. **56**(10): p. 3248-3252.
- [13] Weiss, H.S.H.S.P., A charge simulation method for the calculation of high voltage fields. *IEEE PAS*, pp1660-1668, 1974.
- [14] Schelkunoff, S.A., The electromagnetic theory of coaxial transmission lines and cylindrical shields. *Bell Labs Technical Journal*, 1934. **13**(4): p. 532-579.
- [15] Li, B., Du, Y. and Chen, M., Thin-wire models for inclined conductors with frequency-dependent losses. *IEEE Trans. on PWRD*, 2019. **35**(3): p. 1083-1092.
- [16] Toh, T.-C., *Electromagnetic Theory for Electromagnetic Compatibility Engineers*. 2013: CRC Press.
- [17] Fu, F., Tang, X., *Asynchronous Motor Design Manual* (in Chinese). 2002: China Machine Press.
- [18] Du, Y., Li, B. and Chen, M., Surges induced in building electrical systems during a lightning strike. *Electric Power Systems Research*, 2016. **139**: p. 68-74.
- [19] Ammon, R., et al., *Guide for improving the lightning performance of electric power overhead distribution lines-IEEE Standard*, New York. 1997.
- [20] Epcos, A., *Data Book for SIOV Metal Oxide Varistors*. Munich, Germany: Epcos AG, 2008.
- [21] Tatematsu, A. and Noda, T., Three-dimensional FDTD calculation of lightning-induced voltages on a multiphase distribution line with the lightning arresters and an overhead shielding wire. *IEEE Trans. on EMC*, 2014. **56**(1): p. 159-167.
- [22] Baba, Y. and Rakov, V., On the transmission line model for lightning return stroke representation. *Geophysical Research Letters*, 2003. **30**(24).
- [23] *Railway applications - Insulation coordination. Part 2: Overvoltages and related protection. Standard EN 50124-2*, 2017.
- [24] Commission, I.E., *Protection against lightning, Part 1: General principles. IEC 62305-1*, 2004.
- [25] Littelfuse, I., *Littelfuse Varistor HA Datasheet*. 2020.
- [26] Du, Y. and Xia, N., Principles of power - frequency magnetic shielding with finite - width plates. *International Transactions on Electrical Energy Systems*, 2014. **24**(8): p. 1168-1184.
- [27] Xia, N. and Du, Y., An efficient modelling method for 3-D magnetic plates in magnetic shielding. *IEEE Trans on EMC*, 2014, **56**(3), p. 608-614.